Interface Engineered Organic Near-Infrared Photodetector for Imaging Applications

Abu Bakar Siddik[1, 2]*, Epimitheas Georgitzikis[1]*, Yannick Hermans[1], Jubin Kang[1,4], Joo Hyoung Kim[1], Vladimir Pejovic[1,2], Itai Lieberman[1], Pawel E. Malinowski[1], Andriy Kadashchuk[1,3], Jan Genoe[1,2], Thierry Conard[1], David Cheyns[1] and Paul Heremans[1,2].

[1]IMEC, Kapeldreef 75, 3001 Leuven, Belgium.

[2]Department of Electrical Engineering ESAT, KU Leuven, Kasteelpark Arenberg 10, 3001 Leuven, Belgium.

[3]Institute of Physics, National Academy of Sciences of Ukraine, Prospect Nauky 46, 03028 Kyiv, Ukraine.

[4]Department of Electrical Engineering, Ulsan National Institute of Science and Technology, Ulsan 44919, South Korea.

KEYWORDS

Near-infrared photodetector, dark current density, response time, a-IGZO, activation energy, Q-DLTS, Poole-Frenkel emission, image sensor

ABSTRACT

We report a high-speed low dark current near-infrared (NIR) organic photodetector (OPD) on silicon substrate with amorphous indium gallium zinc oxide (a-IGZO) as electron transport layer (ETL). In-depth understanding on the origin of dark current is obtained using an elaborate set of characterization techniques, including temperature-dependent current-voltage measurements, current-based deep-level transient spectroscopy (Q-DLTS) and transient photovoltage (TPV) decay measurements. These characterization results are complemented by energy band structures deduced from ultraviolet photoelectron spectroscopy (UPS). The presence of trap states and a strong dependency of activation energy on the applied reverse bias voltage point to a dark current mechanism based on trap-assisted field-enhanced thermal emission (Poole-Frenkel emission). We significantly reduce this emission by introducing a thin interfacial layer between the donor: acceptor blend and the a-IGZO ETL, and obtain a dark current as low as 125 pA/cm^2 at an applied reverse bias of -1 V. Thanks to the use of high-mobility metal-oxide transport layers, a fast photo response time of 639 ns (rise) and 1497 ns (fall) is achieved, which, to the best of our knowledge, is among the fastest reported for NIR OPDs. Finally, we present an imager integrating the NIR OPD on a CMOS Read-Out Circuit (ROIC), demonstrating the significance of the improved dark current characteristics in capturing high-quality sample images with this technology.

1. INTRODUCTION

After decades of parallel development with organic photovoltaics, organic photodetectors (OPDs) have become one of the key candidates for photo-sensing applications including imaging, optical communication, industrial sorting, environmental and biomedical monitoring,

and artificial vision.[1–5] High-performance ultraviolet (UV) and visible light (VIS) OPDs are demonstrated.[4–7] With higher information depth, NIR light sensing is particularly interesting for next-generation automotive and biological imaging, however, the effort towards developing high-performance NIR OPDs has remained rather limited compared to UV-VIS.[8–10] To date, the NIR imaging and sensing industry is dominated by epitaxially grown crystalline III-V semiconductors such as InGaAs and HgCdTe.[10–13] However, III-V photodetector diode arrays require flip-chip bonding at the chip level to read-out ICs to make imagers, which results in costly assembly and limited pixel pitch (typically 5-10 μm).[12–14] Therefore, alternative semiconductors for NIR detection are being pursued. One such alternative photodetector is based on colloidal quantum dots (QDs) such as PbS, HgTe, and InAs[12,13,15] while other photodetectors are based on metal-free organic semiconductors[3–5,11], utilized in this work.

The reverse dark current density (J_D) negatively influences the specific detectivity (D*) of a photodetector as it is one of the dominant contributors to the noise current.[16–19] Therefore, it is important to improve the understanding of dark current mechanisms. The dark current density in organic photodetectors is predominantly attributed to either bulk thermal generation within the photoactive layer or charge carrier injection from metal electrodes.[1,10,11,16,17] Although most of the studies on the intrinsic origin of J_D primarily focus on OPDs with UV-VIS materials, recent reports[17–19] include NIR absorbers, expose a discrepancy between the experimentally measured and the theoretically expected dark current by band-to-band thermal generation. The presence of energetically disordered states and distributed trap states in the D-A blend are the most likely reasons for the deviation of J_D from its ideal value.[17–19] Therefore, it is crucial to quantify the trap states and understand how the traps affect the performance of OPDs.

The two key performance parameters of fast photodetectors are the optical response time (typically measured in terms of rise and fall times) and responsivity (R). The response time of organic photodetectors is usually slow because of the low carrier mobility of organic semiconductors (both in the organic absorber and in transport layers) in the OPD stack.[1,20] One way to improve the response time is by using inorganic semiconductors with higher mobility (>1 cm^2/Vs) for the transport layers (both for electrons and holes).[21–23] Recent reports on high-speed photodetectors suggest that combining organic bulk heterojunction (BHJ) and organic-inorganic hybrid perovskite (OIHP) can be another way to improve the optical response time, however with an increased dark current compared to pure OPDs.[24,25] Therefore, devices with both low dark current (< 1 nA/cm^2) and fast response time (< 1 μs) are yet to be achieved.

Herein, we report high-speed low dark current organic photodetectors with amorphous indium gallium zinc oxide (a-IGZO) as the electron transport layer (ETL). The OPD with a-IGZO as ETL reaches a fast rise time of 607 ns and a fall time of 1163 ns, however, we observe a high reverse dark current density of 4.26 μA/cm^2 at -3.50 V. To achieve a NIR OPD with both fast response time and low dark current density (< 1 nA/cm^2), we introduce a thin interfacial layer of co-evaporated C60:LiF between the organic bulk heterojunction (BHJ) and a-IGZO. This reduces the dark current density by more than three orders of magnitude. We find a trap density of ~$9.59 \times 10^{16} cm^3$ at an energy depth of ~0.30 eV for the OPD without interfacial layer. We infer that these traps at the interface between organic BHJ and a-IGZO play a major role in assisting thermally-generated dark current without the interfacial layer. This study brings a good insight into the dark current mechanism in NIR OPD by presenting a detailed characterization of trap states, temperature-dependent current-voltage (J-V) characteristics, and energy band structure models of both OPD stacks. We also demonstrate imagers based on these two devices,

where the device with the interfacial layer can capture high-quality images benefiting from the low dark current.

2. RESULTS AND DISCUSSION

2.1 Device characterization

Figure 1a shows the schematic diagram of the NIR OPD stack using a-IGZO as ETL. It comprises, from bottom to top: a patterned TiN bottom electrode, an a-IGZO layer (ETL), the organic bulk heterojunction (BHJ) with PTB7-th and IEICO-4f (donor-acceptor (D-A)), MoOx (HTL), and ITO as transparent top electrode. The current-voltage characteristics (J-V) under dark and NIR light (~927 W/m^2 at 943 nm) in Figure 1b exhibit a reverse dark and photocurrent density of 4.26 µA/cm^2 and 6.16 mA/cm^2, respectively at −3.50 V. The high photocurrent density of 6.16 mA/cm^2 suggests the good absorption of NIR light by the organic D-A pair and favorable energy band alignment for photogenerated carrier extraction. The EQE of ~57% at 900 nm (Figure 1c) is in line with previous reports using the same organic D-A pair.[11,26–28] EQE at 900 nm as a function of applied reverse bias voltages (Figure 1d) demonstrates that the device
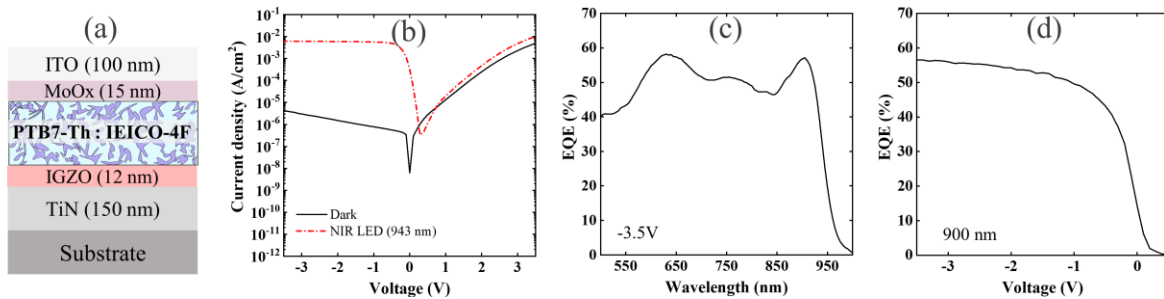

Figure 1. (a) Schematic diagram of OPD with a-IGZO as ETL. (b) J-V characteristics under dark and NIR light, and EQE as a function of wavelength and reverse bias voltages in (c)-(d), respectively.

can deliver ~50% EQE down to −1.0 V. To address the origin of high dark current using a-IGZO as ETL, we fabricate an OPD with TiO_2 as ETL to replace the a-IGZO layer. Although both a-IGZO and TiO_2 show favorable energy structure (Figure S1, SI) to extract electrons from the BHJ via the LUMO level of IEICO-4f (BHJ acceptor molecule), the OPD with TiO_2 shows almost 2 orders of magnitude lower dark current compared to that with a-IGZO as ETL (Figure S2). This indicates that the energy band offset is not the reason behind the origin of high dark current using a-IGZO as ETL. Instead, we hypothesize that the high dark current is the result of a high trap density at the a-IGZO/BHJ interface.

To improve the quality of the a-IGZO/BHJ interface we introduce a thin (7 nm) interfacial layer of co-evaporated C60 and LiF (C60:LiF) between the BHJ and a-IGZO layers. A detailed characterization of the C60:LiF layer can be found in our previous report,[11] where we
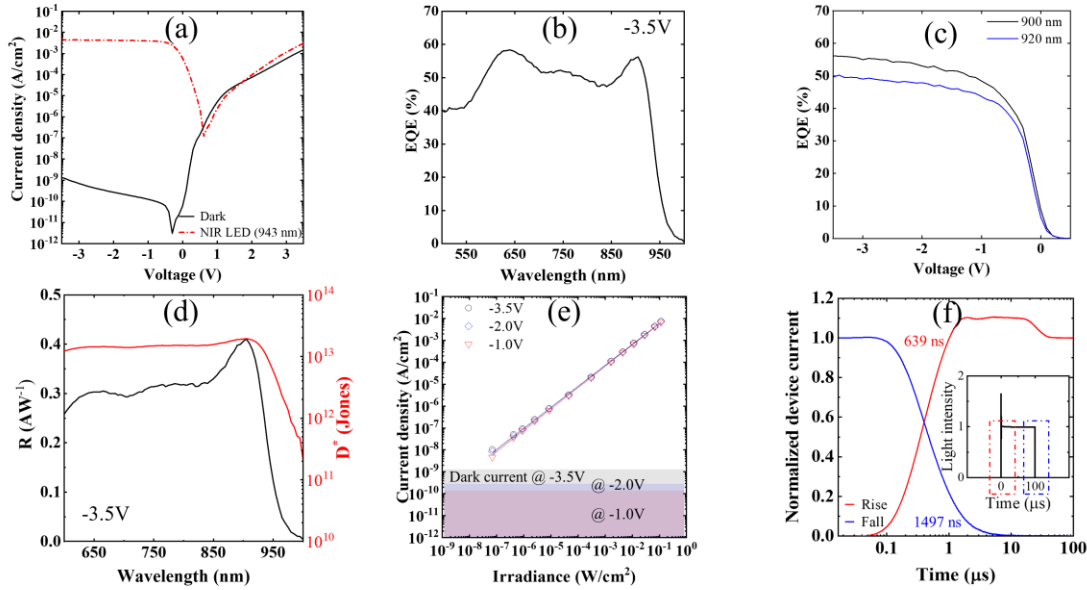

Figure 2. (a) Dark and NIR photocurrent density of OPD with IGZO-C60:LiF. (b) EQE profile as a function of wavelength at −3.5 V. (c) EQE vs voltage at 900 and 920 nm. (d) Responsivity (black) and shot noise limited specific detectivity D* as a function of wavelength (e) Evolution of current density with applied illumination at different reverse biases of −3.5, −2 and −1 V (f) Transient photocurrent (TPC) shows the rise and fall times of the OPD (inset: the utilized NIR light pulse).

demonstrated that a C60:LiF layer can passivate trap states. The dark J-V characteristic of the OPD with a LiF:C60 interfacial layer between the BHJ blend and the a-IGZO ETL, reported in Figure 2a, shows a low dark current density of 1.33 nA/cm^2 at -3.5 V which is one of the lowest ever reported for a NIR OPD. Operating the OPD at biases of -2 V and -1 V even yields a J_D of 270 pA/cm^2 and 125 pA/cm^2, respectively. To further strengthen our claim of low dark current with this NIR OPD stack, we present dark J-V characteristics of 10 devices from a substrate in Figure S3a, showing good uniformity. A high NIR photocurrent density of 4.42 mA/cm^2 in Figure 2a shows 6.52 orders of magnitude jump from the corresponding dark current at -3.5 V which confirms that the C60:LiF interfacial layer does not have negative impact on the photogenerated carrier extraction. Over 50% EQE can be seen throughout the spectral range of 600-920 nm, peaking at ~55% EQE at 900 nm (Figure 2b). EQE vs wavelength uniformity is also evident in Figure S3b. Figure 2c shows that the EQE is relatively constant over a wide range of applied reverse biases (-1 to -3.5 V), which is important for integrating the photogenerated charge carriers in a read-out IC for imaging applications[12,14] The high EQE in the NIR region and low dark current density of the OPD result in a high responsivity of 0.41 AW^{-1} at ~900 nm and $>10^{13}$ Jones of shot-noise limited specific detectivity (D*), shown in Figure 2d. The photocurrent density as a function of the irradiance is a crucial measure for the linearity of the photo response of a photodetector. We observe a good linearity of the reversed biased OPD at -3.5 V, -2.0 V, and -1.0 V upon illuminating under a white LED light in Figure 2e.

One of the key achievements of this NIR OPD is the fast response time of transient photocurrent (TPC) measured by the standard square wave method.[29,30] We utilize a NIR light (peaking at 943 nm) pulse of 100 μs of ~927 W/m^2 to record the transient rise and fall times (10% to 90% of the steady state signal and vice-versa) of the photocurrent. Figure 2f shows the measured rise and

fall times of 639 ns and 1497 ns, respectively, which, to the best of our knowledge, are amongst the fastest reported for NIR OPDs.[6,11,31–34] Comparing this rise/fall (639/1497 ns) time with a-IGZO-only OPD (607/1163 ns) in Figure S4f, we show that the response speed is well maintained when introducing the interfacial layer. We compare dark and NIR light illuminated current density, EQE vs wavelength, EQE vs voltage, responsivity, shot noise limited specific detectivity (D*) and TPC rise/fall times of both OPD with and without C60:LiF interfacial layer together in Figure S4 and further confirm that the OPD with IGZO-C60:LiF shows large improvement over the IGZO-only OPD in terms of D* benefiting from the low dark current while still delivers similar EQE, responsibility and TPC response speed. All the parameters of Figure S4 are also summarized in Table S1.

To explain the origin of the low dark current, we first look at the complete energy band diagram, deduced from ultraviolet photoelectron spectroscopy (UPS). Each layer of the stack (Figure 3a) is characterized by UPS to extract secondary cut-off and valence band positions, as can be seen in Figure 3b. Figure S5 shows the detailed procedure to calculate ionization energy and work
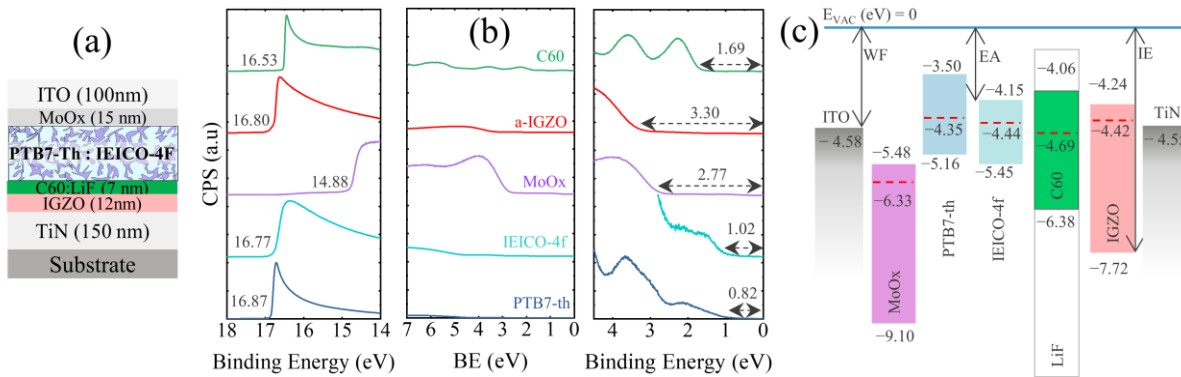

Figure 3. (a) Schematic diagram of OPD stack with IGZO-C60:LiF. (b) UPS spectra of PTB7-th, IEICO-4f, MoOx, a-IGZO, and C60 exhibiting secondary electron cutoff and valence level energy. (c) Complete energy band diagram of the OPD stack referenced to the vacuum energy level.

function from the extracted cut-off and valence band position. The electron affinity is adapted by adding the bandgap of each layer obtained by absorption spectroscopy. The complete energy band diagram of the OPD stack referenced to the vacuum energy level in Figure 3c indicates the presence of an energy barrier between the BHJ acceptor molecule IEICO-4f and the C60 LUMO level. The Fermi-referenced energy band diagram (Figure S6) confirms this intrinsic energy barrier at thermal equilibrium as ~0.30 eV, which can restrict the electron flow from the BHJ materials to a-IGZO at the reverse dark condition. This partially explains why we achieve a lower dark current using an interfacial layer.

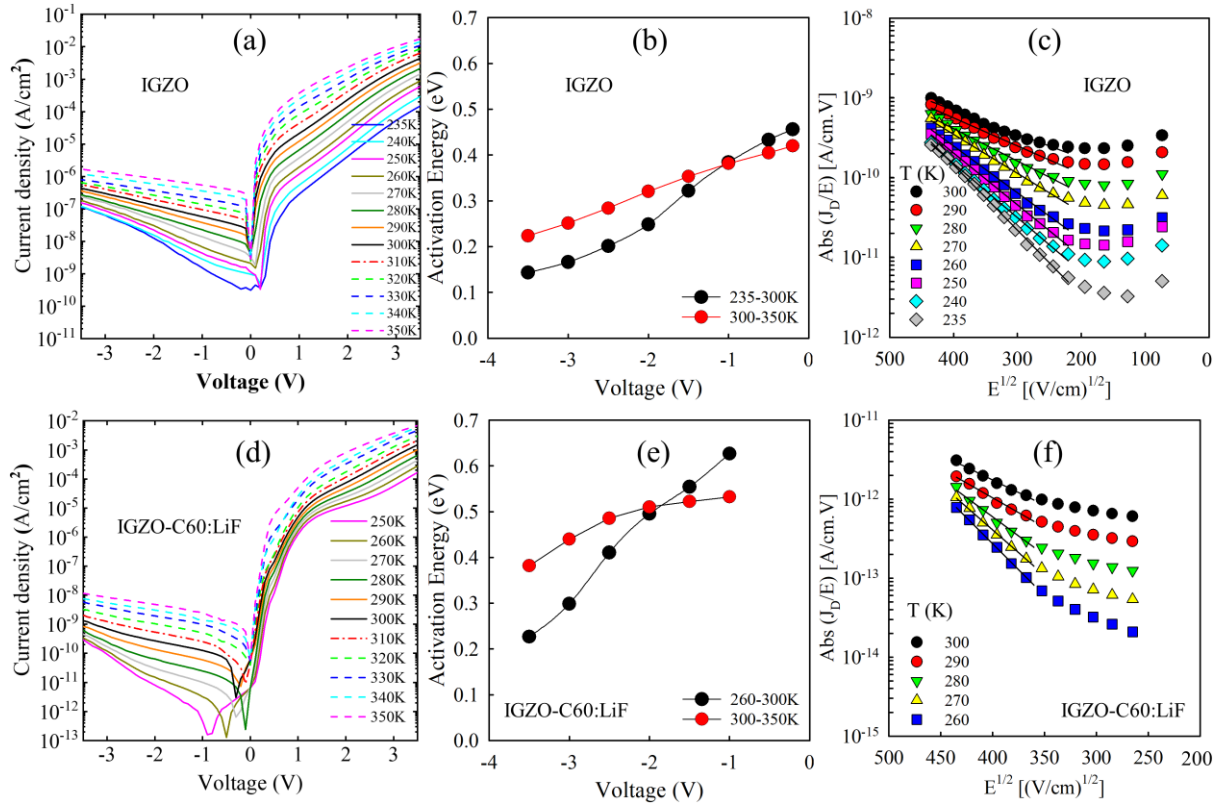## 2.2 Investigation on the origin of dark current

Figure 4. Temperature-dependent dark J-V characteristics, activation energies of 2 different temperature ranges from respective Arrhenius plots, and Poole-Frenkel plot (ln(J/E) vs $\sqrt{E}$) for IGZO-only OPD and OPD with IGZO-C60:LiF are in (a)-(c) and (d)-(f), respectively.

We carry out temperature-dependent dark J-V measurements on devices with a-IGZO as ETL, both with and without the interfacial layer, to study the effect of temperature and bias on reverse dark current. To avoid confusion and allow a smooth reading experience, from now on we refer to these devices as "IGZO-only OPD" (Figure 1a) and "OPD with IGZO-C60:LiF" (Figure 3a). The dark current of the IGZO-only OPD shows a strong temperature dependency (Figure 4a), especially at small reverse bias voltages (0 to −1.0 V), exhibiting low dark current at low temperatures. This large temperature dependency of the reverse dark current for this voltage range over the temperature range 235 K to 300 K indicates that thermal assistance plays a big role in the origin of high dark current. However, when further increasing the reverse bias (>1 V), the dark current shows greater dependency on the electric field. This indicates that both temperature and field contribute to the origin of dark current, therefore, it is worth looking at the activation energies for 2 different temperature ranges, namely 235-300 K and 300-350 K. The activation energies (E_a) of the IGZO-only OPD devices from Arrhenius plots (shown in Figure S7a-b) in the range 235-300 K and 300-350 K are plotted versus the reverse bias in Figure 4b. For the applied reverse bias range −0.20 to −3.5 V, E_a in Figure 4b changes from 0.46 eV to 0.13 eV in the temperature range 235-300 K and from 0.42 eV to 0.22 eV in the range 300-350 K. In both temperature ranges, this means that both the electric field and temperature contribute to the dark current mechanism. However, the field activation of the dark current becomes more prominent at −3.5 V at lower temperatures (235-300 K), having a smaller activation energy of 0.13 eV (compared to 0.22 eV at elevated temperatures 300-350 K), since the thermal contribution becomes smaller at low temperature.[18]

Kublitski et al. calculated thermally-generated dark current (J_0) within the radiative limit as a function of charge-transfer state energy (E_{CT}) of various organic D-A blends (a J_0 of ~10^{-12}

A/cm^2 was calculated for D-A blend of similar E$_{CT}$ of ~1.1 eV to this work), where J$_0$ was found to be several orders of magnitude lower than the experimentally measured J$_D$.[19] Several key works on the origin of dark current reported the presence of traps within the D-A blend interfaces and energy disorder of organics as the primary source of the large discrepancy between the experimentally measured and the ideal thermally-generated dark current.[17–19] Herein, we obtain a maximum activation energy of 0.46 eV at −0.2 V, which is well below the E$_{CT}$ of ~1.1 eV. This suggests that the thermal generation of CT states is highly unlikely. We propose that the carriers (electrons in this case) can thermally emit from the BHJ via trap states within the BHJ D-A blend or D-A/IGZO interface to the IGZO.[18,19] In the presence of electric field, this carrier emission process can be enhanced[35,36], a process known as Poole-Frenkel emission. A linear relation between ln(J/E) and $\sqrt{E}$ (Poole-Frenkel (P-F) plot) is widely considered as the evidence of field-enhanced emission.[18,35,37] OPD with IGZO exhibits a linear P-F region (Figure 4c) between 230-435 (V/cm)$^{1/2}$ which corresponds to the reverse bias voltages between −1.0 to −3.5 V. This linearity agrees with the temperature-dependent J-V curves and the field-dependent activation energy plot. The ln(J/E) is independent of $\sqrt{E}$ for smaller reserve bias (<1 V), which reveals the electric field has very little to no influence on the activation barrier, so J$_D$ is rather thermally activated in this region.

Thanks to the interfacial layer C60:LiF, the dark current of the device approaches the thermal limit[19] (~10^{-12} A/cm^2) at low temperatures and low reverse biases (=<1 V). As mentioned earlier, the C60 LUMO level introduces an intrinsic energy barrier of 0.30 eV to the LUMO of acceptor IEICO-4f, which results in a higher emission barrier. Thus, the probability of carrier emission via this interface becomes lower and we achieve ~10^{-12} A/cm^2 at low temperatures and low biases. The activation energy in Figure 4e still shows dependency on the electric field, however, a high

activation energy of 0.64 eV at −1.0 V for the OPD with IGZO-C60:LiF (compared to 0.37 eV for the IGZO-only OPD) indicates a reduced field effect. The linearity of P-F plot at ≥370 $(V/cm)^{1/2}$ in Figure 4f further confirms the reduced field effect.

To further elucidate the mechanism of the dark current generation, we next characterize the trap states that facilitate field-enhanced thermionic emission.[35–37] Several groups have successfully employed current-based deep-level transient spectroscopy (Q-DLTS) to quantify deep-lying trap states in PbS nanocrystals treated with organic ligands, organic semiconductors, and perovskites.[38–40] Herein, we utilize Q-DLTS to characterize the trap states (including trap emission density ($N_{E,T}$), trap activation energy (ΔE_T) and capture cross-section (σ_T)) within our OPD stack with IGZO. All equations used for Q-DLTS analysis are denoted in note 1, SI, which
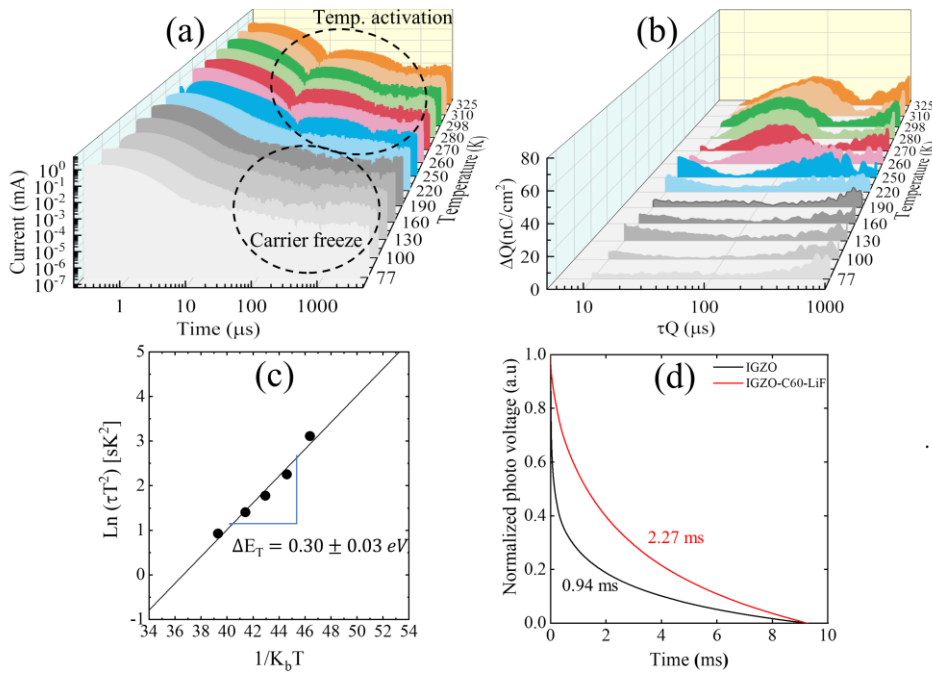

Figure 5. (a) Temperature-dependent transient current exhibiting trap emission current $J_E(t)$ features. (b) Q-DLTS spectra (ΔQ) for varying different time constants (τ_Q) at different temperatures (c) Trap activation energy from linear fit of Arrhenius plot connecting the (ΔQ) peak points with corresponding τ_Q and temperatures. (d) Normalized TPV of IGZO-only OPD and OPD with IGZO-C60:LiF.

are adapted from the report of Bozyigit et al.[38] We apply a constant reverse V_D of -1.2 V to the OPD and then switch the V_D to 0 V for 10 ms to monitor the transient current $J_D(t)$ characteristics. During the first transition from -1.2 to 0 V, the traps within the depletion region are filled by charge carriers, which are then emitted during the next transition of the pulse from 0 to -1.2 V in order to achieve a new thermal equilibrium.[38] Temperature activation is evident from the transient current plot of the OPD in Figure 5a from 325 to 220 K. Prior to calculating the DLTS spectra (ΔQ) (equation 5 in note 1, SI), the trap emission current density $J_E(t)$ is calculated from the transient current in Figure 5a by subtracting the capacitive displacement current and steady-state dark current. We calculate ΔQ for the timeframe between 10 μs and 1 ms, which defines the detector time constant (τ_Q) (equation 6 in note 1 SI).[38] The resulting temperature-activated Q-DLTS spectra (ΔQ) for 298-77 K (Figure 5b) show a peak shift towards longer τ_Q as the de-trapping process becomes slower with decreasing temperature, and eventually, the peak disappears after 220 K as the carriers freeze out.[38,41] Going beyond room temperature, the peak moves to longer τ_Q (slower de-trapping process), which might be caused by multiple trapping de-trapping cycles at elevated temperatures.[42] Figure 5c demonstrates the Arrhenius plot of time constants corresponding to the Q-DLTS peaks at respective temperatures (250-298 K). The linear fit of the Arrhenius plot reveals a trap activation energy of ~0.30 eV and a capture cross-section (σ_T) of ~1.75×10^{-16}cm^2 (SI, equations 3 and 6). We calculate a trap density ($N_{T,298K}$) of ~9.59×10^{16}cm^3 at 298 K (SI, equation 4). To further verify the presence of trap states we perform transient photovoltage decay (TPV) under the open-circuit condition, where a faster charge-recombination lifetime relates to a higher trap density.[43,44] A charge-recombination lifetime of 0.94 ms for IGZO-only OPD compared to 2.27 ms for OPD with IGZO-C60:LiF validates the trap quantification by Q-DLTS in terms of the presence of active

traps at the a-IGZO/BHJ interface. The Q-DLTS spectra for the OPD with IGZO-C60:LiF in Figure S8 exhibit no temperature activation. This verifies the long carrier lifetime of 2.27 ms using the interfacial layer and proves our hypothesis on improving the quality of the interface in terms of reduced trap density.

By now combining the energy band diagram measured by UPS with the findings of temperature-dependent J-V, Q-DLTS, and TPV measurements, we can present in Figure 6 a picture of the reverse-biased band diagrams under the dark condition and the origin of high dark current. Since we observe the presence of high trap density in IGZO-only OPD by Q-DLTS combined with an improved carrier lifetime upon using C60:LiF interfacial layer, we conclude that the trap density of $\sim 9.59 \times 10^{16} \, cm^3$ at ~ 0.30 eV depth is located at the a-IGZO/BHJ interface as shown in Figure 6a. In the dark under the smaller reverse bias (Figure 6a), electrons from the IEICO-4f HOMO level can be thermally emitted via trap sites at the interface and reach the IGZO conduction band.
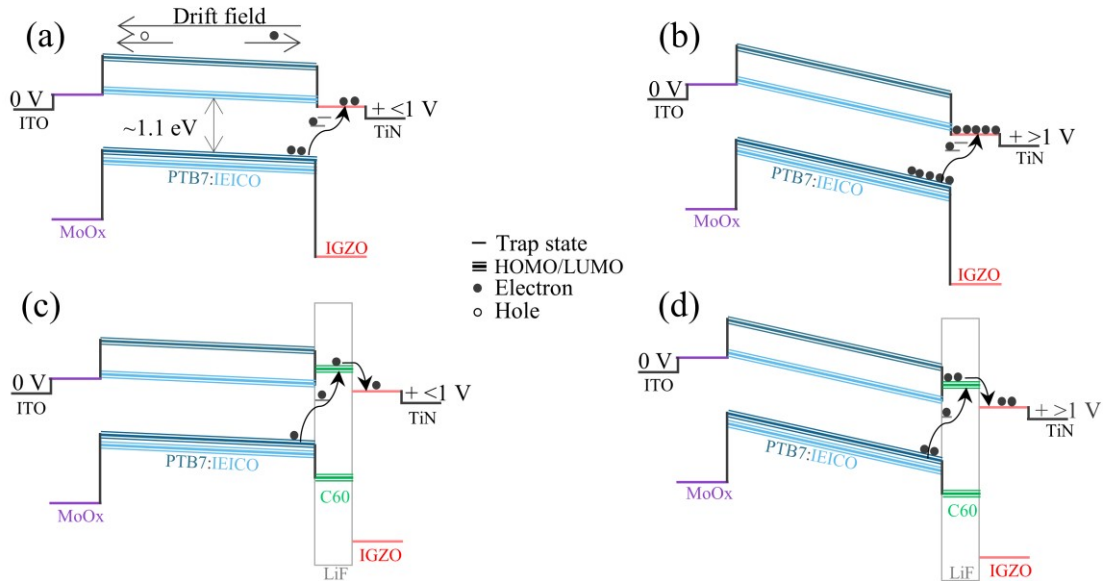

Figure 6. Carrier dynamics derived from Fermi-refenced energy band diagram under dark condition at two different applied reverse bias voltage ranges, (a)-(b) for IGZO-only OPD and (c)-(d) for OPD with IGZO-C60:LiF.

On the other hand, the corresponding holes can readily travel to the MoOx layer via the PTB7-th HOMO level, where they most likely recombine with electrons from the conduction band of MoOx[45], which is balanced by subsequent electron injection from the ITO electrode. Increasing reverse bias voltage will amplify the number of thermally ejected electrons (Figure 6b) by lowering the emission barrier as explained earlier from both P-F and field-dependent activation energy plots. In the device with LiF:C60 interfacial layer (Figure 6c), the LUMO to reach for trap-assisted thermionic-emitted electrons from the IEICO-4f HOMO level is 0.30 eV higher, and moreover, the trap density to assist that thermionic emission is lower. That explains the low dark current density J_D ~125 pA/cm^2 at -1 V. However, for this device, we observe linearity in $\ln(J/E)$ vs $\sqrt{E}$ for reverse bias ≥ 3 V, which suggests that a small number of carriers can thermally emit under a high field (Figure 6d).
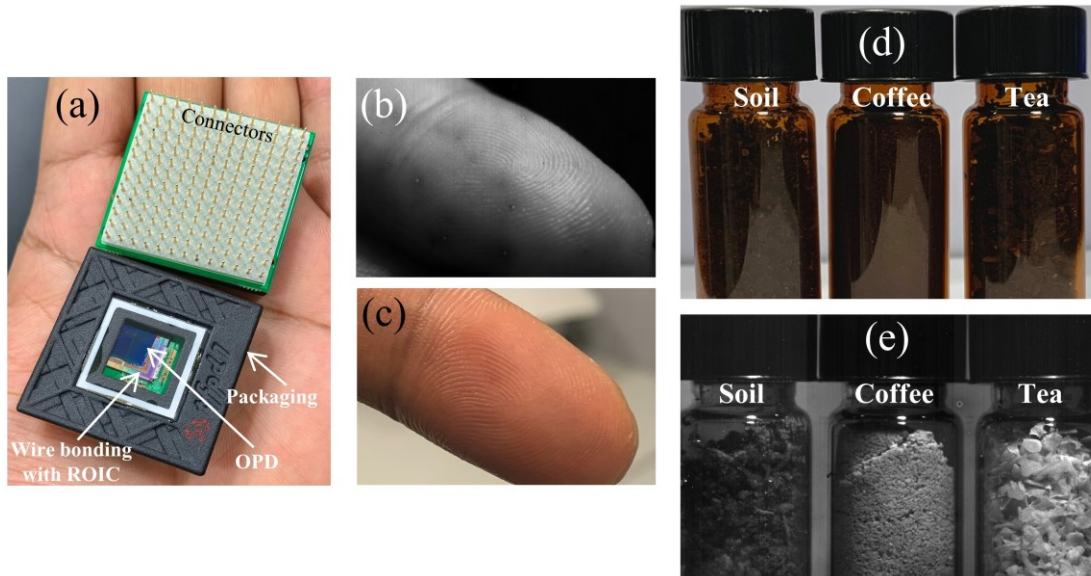

Figure 7. (a) OPD imager chip. Images of fingertip captured by our optimized OPD (with interfacial layer) imager (b) and by smartphone (c). Unlike visible imaging with smartphone (d), looking through the brown vials with OPD NIR imaging (e) reveals significant contrast difference between soil, coffee, and tea.

15

2.3 Application: OPD imager on Si read-out IC

To demonstrate NIR imagers, we monolithically integrate an array of OPDs on a CMOS read-out IC (ROIC), designed and fabricated in 130 nm technology. The CMOS ROIC features 3-transistor (3T) architecture, 5 μm pixel pitch and the array consists of 512×768 pixels. Light impinges from the top transparent ITO electrode and the electrons are collected at the bottom contact, then transferred to the read-out IC and integrated into a storage capacitor to be converted into a voltage at the sensing node. Figure 7a displays a photograph of the imager chip. We measure dark currents of 2.90 μA/cm^2 for IGZO-only OPD, and 38.7 nA/cm^2 (Read-out IC pixel architecture limited) for OPD with IGZO-C60:LiF at -3.3 V, which correspond well to the device level dark currents mentioned earlier. Pictures taken by these two imagers, shown in Figure S9a-b, clearly reveal the benefit of low dark current, as the OPD imager with high dark current struggles to attain any detail (Figure S9a) due to low signal-to-noise ratio. On the other hand, pictures captured by OPD with low dark current (high signal-to-noise ratio) in Figure 7b and Figure S9b exhibit good contrast and detail (reference pictures taken by smartphone camera, Figures 7c and S9c). Having longer wavelengths, NIR light has certain advantages as it can reveal distinctive details that cannot be resolved by visible imaging.[11] We show an example in Figure 7d-e. The smartphone camera struggles to acquire information through a semi-transparent brown vial and offers only a poor contrast between soil, coffee, and tea (Figure 7d). On the contrary, NIR imaging with our optimized OPD retrieves rich information through the brown glass and shows substantial contrast differences between soil, coffee, and tea (Figure 7e).

3. CONCLUSIONS

We present a NIR OPD stack with low dark current density (<1 nA/cm^2) over a wide range of applied reverse bias voltages, high EQE of over 50% (900-910 nm), and fast response time. We present a model for dark current generation by combining UPS, temperature-dependent J-V characteristics, Q-DLTS, and TPV measurements, that explains the effect on the dark current upon adding a thin LiF:C60 layer between the bulk heterojunction active layer and the IGZO ETL layer of our photodiodes. We integrate our OPD on a CMOS read-out IC to create a NIR imager and show the benefit of the low dark current for capturing high-contrast fine detail images.

4. EXPERIMENT

We prepared isolated films on gold (Au) coated silicon substrates for ultraviolet photoelectron spectroscopy (UPS) measurements, which were carried out using a PHI 5000 VersaProbe tool equipped with a photon beam of 21.2 eV (He I) from Physical Electronics. Prior to recording sample spectra, the spectrometer was calibrated with Ag foil to determine the Fermi energy reference, and a sample bias of -5 V was applied during all the measurements to detect the secondary electron (SE) emission edge. Sputter cleaning was carried out on the samples using a gas cluster Ar beam (GCIB) at 2.5 KV energy/atom for 30 s to remove surface hydrocarbon. Post-processing of spectra was performed using MultiPak (data reduction software for XPS and AES by ULVAC-PHI).

For OPDs, first, a silicon substrate with a pre-pattern TiN bottom electrode was cleaned in an ultrasonic bath with acetone and isopropyl alcohol. Then, IGZO was sputtered from a target with In:Ga:Zn ratio 1:1:1, and subsequently patterned by photolithography to form islands. A co-evaporated thin layer of C60 and LiF with an evaporation rate ratio of 1:4 was deposited using an

Angstrom evaporation tool. Active layer PTB7-th/IEICO-4f was spin-coated at 1000 rpm for 60s from a 20 mg mL^{-1} solution with a ratio of 1:1.5 by weight in chlorobenzene. The chemical formulas of PTB7-th and IEICO-4f can be found elsewhere.[11] HTL MoOx and transparent top electrode ITO were deposited by thermal evaporation and sputtering, respectively.

To develop the imager, we started from a custom-designed readout IC (ROIC) in 130-nm CMOS technology, that features arrays containing 768×512 pixels with a pixel pitch of 5 μm. A 3T pixel readout architecture was used and pixel outputs were buffered and serially multiplexed on chip, then digitized by on-board 16-bit analog-to-digital converter (ADC). More details on the pixel architecture can be found in our previous report[14]. The processing of the organic photodetector stack was carried out on chip level. First, the ETL IGZO was deposited using a shadow mask. Then, C60 and LiF were co-evaporated as the interfacial layer using the same shadow mask. The organic layer PTB7-th/IEICO-4f was spin-coated and carefully scratched out to expose the contact areas. Both HTL and top electrode were also deposited using shadow masks. Finally, the obtained OPD image sensor was wire bonded to a printed circuit board and packaged for testing as shown in Figure 7a.

We refer to our previous report for the characterization detail of J-V and EQE.[11]

Temperature-dependent J-V characteristics were measured with an Agilent 4156 semiconductor parameter analyzer in the dark paired with a cryostat from Lake Shore Cryotronics, Inc. Current based deep-level transient spectroscopy (Q-DLTS) and transient photovoltage (TPV) decay measurements were performed using Paios System (Fluxim AG, Switzerland). The system was paired with a cryostat from Lake Shore Cryotronics, Inc. for Q-DLTS.

Supporting Information

Energy band alignment, device schematics, J-V characteristics, EQE, responsivity, shot noise limited specific detectivity, TPC, UPS, Arrhenius plots, Q-DLTS spectra, OPD imager, Q-DLTS equations

AUTHOR INFORMATION

Corresponding Authors

Abu Bakar Siddik- IMEC, Kapeldreef 75, 3001 Leuven, Belgium, and Department of Electrical Engineering ESAT, KU Leuven, Kasteelpark Arenberg 10, 3001 Leuven, Belgium.

abu.bakar.siddik@imec.be

Epimitheas Georgitzikis- IMEC, Kapeldreef 75, 3001 Leuven, Belgium.

epimitheas.georgitzikis@imec.be

Author Contributions

The manuscript was written through contributions of all authors. All authors have given approval to the final version of the manuscript.

Notes

The authors declare no competing financial interest.

REFERENCES

(1)   Ren, H.; Chen, J.; Li, Y.; Tang, J. Recent Progress in Organic Photodetectors and Their Applications. *Advanced Science* **2021**, *8* (1), 2002418. https://doi.org/10.1002/advs.202002418.

(2)   Liu, X.; Lin, Y.; Liao, Y.; Wu, J.; Zheng, Y. Recent Advances in Organic Near-Infrared Photodiodes. *J Mater Chem C Mater* **2018**, *6* (14), 3499–3513. https://doi.org/10.1039/C7TC05042A.

(3)   Babics, M.; Bristow, H.; Zhang, W.; Wadsworth, A.; Neophytou, M.; Gasparini, N.; McCulloch, I. Non-Fullerene-Based Organic Photodetectors for Infrared Communication. *J Mater Chem C Mater* **2021**, *9* (7), 2375–2380. https://doi.org/10.1039/D0TC05341D.

(4)   Li, L.; Zhang, F.; Wang, J.; An, Q.; Sun, Q.; Wang, W.; Zhang, J.; Teng, F. Achieving EQE of 16,700% in P3HT:PC71BM Based Photodetectors by Trap-Assisted Photomultiplication. *Sci Rep* **2015**, *5* (1), 9181. https://doi.org/10.1038/srep09181.

(5)   Guo, D.; Yang, L.; Zhao, J.; Li, J.; He, G.; Yang, D.; Wang, L.; Vadim, A.; Ma, D. Visible-Blind Ultraviolet Narrowband Photomultiplication-Type Organic Photodetector with an Ultrahigh External Quantum Efficiency of over 1 000 000%. *Mater Horiz* **2021**, *8* (8), 2293–2302. https://doi.org/10.1039/D1MH00776A.

(6)   Kielar, M.; Dhez, O.; Pecastaings, G.; Curutchet, A.; Hirsch, L. Long-Term Stable Organic Photodetectors with Ultra Low Dark Currents for High Detectivity Applications. *Sci Rep* **2016**, *6* (1), 39201. https://doi.org/10.1038/srep39201.

(7)   Zheng, W.; Lin, R.; Zhang, Z.; Liao, Q.; Liu, J.; Huang, F. An Ultrafast-Temporally-Responsive Flexible Photodetector with High Sensitivity Based on High-Crystallinity Organic–Inorganic Perovskite Nanoflake. *Nanoscale* **2017**, *9* (34), 12718–12726. https://doi.org/10.1039/C7NR04395C.

(8)   Wu, Z.; Zhai, Y.; Kim, H.; Azoulay, J. D.; Ng, T. N. Emerging Design and Characterization Guidelines for Polymer-Based Infrared Photodetectors. *Acc Chem Res* **2018**, *51* (12), 3144–3153. https://doi.org/10.1021/acs.accounts.8b00446.

(9)   Wu, Z.; Yao, W.; London, A. E.; Azoulay, J. D.; Ng, T. N. Elucidating the Detectivity Limits in Shortwave Infrared Organic Photodiodes. *Adv Funct Mater* **2018**, *28* (18), 1800391. https://doi.org/10.1002/adfm.201800391.

(10)   Li, Q.; Guo, Y.; Liu, Y. Exploration of Near-Infrared Organic Photodetectors. *Chemistry of Materials* **2019**, *31* (17), 6359–6379. https://doi.org/10.1021/acs.chemmater.9b00966.

(11)   Yang, W.; Qiu, W.; Georgitzikis, E.; Simoen, E.; Serron, J.; Lee, J.; Lieberman, I.; Cheyns, D.; Malinowski, P.; Genoe, J.; Chen, H.; Heremans, P. Mitigating Dark Current for High-Performance Near-Infrared Organic Photodiodes via Charge Blocking and Defect Passivation. *ACS Appl Mater Interfaces* **2021**, *13* (14), 16766–16774. https://doi.org/10.1021/acsami.1c02080.

(12)   Pejovic, V.; Georgitzikis, E.; Lee, J.; Lieberman, I.; Cheyns, D.; Heremans, P.; Malinowski, P. E. Infrared Colloidal Quantum Dot Image Sensors. *IEEE Trans Electron Devices* **2022**, *69* (6), 2840–2850. https://doi.org/10.1109/TED.2021.3133191.

(13)   Georgitzikis, E.; Malinowski, P. E.; Li, Y.; Maes, J.; Hagelsieb, L. M.; Guerrieri, S.; Hens, Z.; Heremans, P.; Cheyns, D. Integration of PbS Quantum Dot Photodiodes on

Silicon for NIR Imaging. *IEEE Sens J* **2020**, *20* (13), 6841–6848. https://doi.org/10.1109/JSEN.2019.2933741.

(14) Pejovic, V.; Lee, J.; Georgitzikis, E.; Li, Y.; Kim, J. H.; Lieberman, I.; Malinowski, P. E.; Heremans, P.; Cheyns, D. Thin-Film Photodetector Optimization for High-Performance Short-Wavelength Infrared Imaging. *IEEE Electron Device Letters* **2021**, *42* (8), 1196–1199. https://doi.org/10.1109/LED.2021.3093081.

(15) Leemans, J.; Pejović, V.; Georgitzikis, E.; Minjauw, M.; Siddik, A. B.; Deng, Y.; Kuang, Y.; Roelkens, G.; Detavernier, C.; Lieberman, I.; Malinowski, P. E.; Cheyns, D.; Hens, Z. Colloidal III–V Quantum Dot Photodiodes for Short-Wave Infrared Photodetection. *Advanced Science* **2022**, *9* (17), 2200844. https://doi.org/10.1002/advs.202200844.

(16) Simone, G.; Dyson, M. J.; Meskers, S. C. J.; Janssen, R. A. J.; Gelinck, G. H. Organic Photodetectors and Their Application in Large Area and Flexible Image Sensors: The Role of Dark Current. *Adv Funct Mater* **2020**, *30* (20), 1904205. https://doi.org/10.1002/adfm.201904205.

(17) Simone, G.; Dyson, M. J.; Weijtens, C. H. L.; Meskers, S. C. J.; Coehoorn, R.; Janssen, R. A. J.; Gelinck, G. H. On the Origin of Dark Current in Organic Photodiodes. *Adv Opt Mater* **2020**, *8* (1), 1901568. https://doi.org/10.1002/adom.201901568.

(18) Ma, X.; Bin, H.; van Gorkom, B. T.; van der Pol, T. P. A.; Dyson, M. J.; Weijtens, C. H. L.; Fattori, M.; Meskers, S. C. J.; van Breemen, A. J. J. M.; Tordera, D.; Janssen, R. A. J.; Gelinck, G. H. Identification of the Origin of Ultralow Dark Currents in Organic Photodiodes. *Advanced Materials* **2023**, *35* (8), 2209598. https://doi.org/10.1002/adma.202209598.

(19) Kublitski, J.; Hofacker, A.; Boroujeni, B. K.; Benduhn, J.; Nikolis, V. C.; Kaiser, C.; Spoltore, D.; Kleemann, H.; Fischer, A.; Ellinger, F.; Vandewal, K.; Leo, K. Reverse Dark Current in Organic Photodetectors and the Major Role of Traps as Source of Noise. *Nat Commun* **2021**, *12* (1), 551. https://doi.org/10.1038/s41467-020-20856-z.

(20) Chow, P. C. Y.; Someya, T. Organic Photodetectors for Next-Generation Wearable Electronics. *Advanced Materials* **2020**, *32* (15), 1902045. https://doi.org/10.1002/adma.201902045.

(21) Huang, W.; Zhu, B.; Chang, S.-Y.; Zhu, S.; Cheng, P.; Hsieh, Y.-T.; Meng, L.; Wang, R.; Wang, C.; Zhu, C.; McNeill, C.; Wang, M.; Yang, Y. High Mobility Indium Oxide Electron Transport Layer for an Efficient Charge Extraction and Optimized Nanomorphology in Organic Photovoltaics. *Nano Lett* **2018**, *18* (9), 5805–5811. https://doi.org/10.1021/acs.nanolett.8b02452.

(22) Ramírez-Como, M.; Balderrama, V. S.; Sacramento, A.; Marsal, L. F.; Lastra, G.; Estrada, M. Fabrication and Characterization of Inverted Organic PTB7:PC70BM Solar Cells Using Hf-In-ZnO as Electron Transport Layer. *Solar Energy* **2019**, *181*, 386–395. https://doi.org/10.1016/j.solener.2019.02.015.

(23)   Anabestani, H.; Nabavi, S.; Bhadra, S. Advances in Flexible Organic Photodetectors: Materials and Applications. *Nanomaterials* **2022**, *12* (21), 3775. https://doi.org/10.3390/nano12213775.

(24)   Shen, L.; Lin, Y.; Bao, C.; Bai, Y.; Deng, Y.; Wang, M.; Li, T.; Lu, Y.; Gruverman, A.; Li, W.; Huang, J. Integration of Perovskite and Polymer Photoactive Layers to Produce Ultrafast Response, Ultraviolet-to-near-Infrared, Sensitive Photodetectors. *Mater Horiz* **2017**, *4* (2), 242–248. https://doi.org/10.1039/C6MH00508J.

(25)   Li, C.; Wang, H.; Wang, F.; Li, T.; Xu, M.; Wang, H.; Wang, Z.; Zhan, X.; Hu, W.; Shen, L. Ultrafast and Broadband Photodetectors Based on a Perovskite/Organic Bulk Heterojunction for Large-Dynamic-Range Imaging. *Light Sci Appl* **2020**, *9* (1), 31. https://doi.org/10.1038/s41377-020-0264-5.

(26)   Wu, G.; Fu, R.; Chen, J.; Yang, W.; Ren, J.; Guo, X.; Ni, Z.; Pi, X.; Li, C.-Z.; Li, H.; Chen, H. Perovskite/Organic Bulk-Heterojunction Integrated Ultrasensitive Broadband Photodetectors with High Near-Infrared External Quantum Efficiency over 70%. *Small* **2018**, *14* (39), 1802349. https://doi.org/10.1002/smll.201802349.

(27)   Wang, Z.; Ji, J.; Lin, W.; Yao, Y.; Zheng, K.; Liang, Z. Mechanistic Investigation into Dynamic Function of Third Component Incorporated in Ternary Near-Infrared Nonfullerene Organic Solar Cells. *Adv Funct Mater* **2020**, *30* (31), 2001564. https://doi.org/10.1002/adfm.202001564.

(28)   Yao, H.; Cui, Y.; Yu, R.; Gao, B.; Zhang, H.; Hou, J. Design, Synthesis, and Photovoltaic Characterization of a Small Molecular Acceptor with an Ultra-Narrow Band Gap. *Angewandte Chemie International Edition* **2017**, *56* (11), 3045–3049. https://doi.org/10.1002/anie.201610944.

(29)   Dou, L.; Yang, Y.; You, J.; Hong, Z.; Chang, W.-H.; Li, G.; Yang, Y. Solution-Processed Hybrid Perovskite Photodetectors with High Detectivity. *Nat Commun* **2014**, *5* (1), 5404. https://doi.org/10.1038/ncomms6404.

(30)   Reissig, L.; Dalgleish, S.; Awaga, K. A Differential Photodetector: Detecting Light Modulations Using Transient Photocurrents. *AIP Adv* **2016**, *6* (1), 015306. https://doi.org/10.1063/1.4939921.

(31)   Babics, M.; Bristow, H.; Zhang, W.; Wadsworth, A.; Neophytou, M.; Gasparini, N.; McCulloch, I. Non-Fullerene-Based Organic Photodetectors for Infrared Communication. *J Mater Chem C Mater* **2021**, *9* (7), 2375–2380. https://doi.org/10.1039/D0TC05341D.

(32)   Pejović, V.; Georgitzikis, E.; Lieberman, I.; Malinowski, P. E.; Heremans, P.; Cheyns, D. Photodetectors Based on Lead Sulfide Quantum Dot and Organic Absorbers for Multispectral Sensing in the Visible to Short-Wave Infrared Range. *Adv Funct Mater* **2022**, *32* (28), 2201424. https://doi.org/10.1002/adfm.202201424.

(33)   Kublitski, J. Enhancing Sub-Bandgap External Quantum Efficiency by Photomultiplication in Narrowband Organic Near-Infrared Photodetectors; 2022; pp 151–169. https://doi.org/10.1007/978-3-030-94464-3_6.

(34) Wang, Y.; Zhu, L.; Hu, Y.; Deng, Z.; Lou, Z.; Hou, Y.; Teng, F. High Sensitivity and Fast Response Solution Processed Polymer Photodetectors with Polyethylenimine Ethoxylated (PEIE) Modified ITO Electrode. *Opt Express* **2017**, *25* (7), 7719. https://doi.org/10.1364/OE.25.007719.

(35) Ganichev, S. D.; Ziemann, E.; Prettl, W.; Yassievich, I. N.; Istratov, A. A.; Weber, E. R. Distinction between the Poole-Frenkel and Tunneling Models of Electric-Field-Stimulated Carrier Emission from Deep Levels in Semiconductors. *Phys Rev B* **2000**, *61* (15), 10361–10365. https://doi.org/10.1103/PhysRevB.61.10361.

(36) Frenkel, J. On Pre-Breakdown Phenomena in Insulators and Electronic Semi-Conductors. *Physical Review* **1938**, *54* (8), 647–648. https://doi.org/10.1103/PhysRev.54.647.

(37) Jeong, D. S.; Hwang, C. S. Tunneling-Assisted Poole-Frenkel Conduction Mechanism in HfO2 Thin Films. *J Appl Phys* **2005**, *98* (11), 113701. https://doi.org/10.1063/1.2135895.

(38) Bozyigit, D.; Jakob, M.; Yarema, O.; Wood, V. Deep Level Transient Spectroscopy (DLTS) on Colloidal-Synthesized Nanocrystal Solids. *ACS Appl Mater Interfaces* **2013**, *5* (8), 2915–2919. https://doi.org/10.1021/am400326t.

(39) Neugebauer, S.; Rauh, J.; Deibel, C.; Dyakonov, V. Investigation of Electronic Trap States in Organic Photovoltaic Materials by Current-Based Deep Level Transient Spectroscopy. *Appl Phys Lett* **2012**, *100* (26), 263304. https://doi.org/10.1063/1.4731637.

(40) Hsieh, H.-C.; Hsiow, C.-Y.; Lin, K.-F.; Shih, Y.-C.; Wang, L.; Renaud, C.; Nguyen, T.-P. Analysis of Defects and Traps in N–I–P Layered-Structure of Perovskite Solar Cells by Charge-Based Deep Level Transient Spectroscopy (*Q* -DLTS). *The Journal of Physical Chemistry C* **2018**, *122* (31), 17601–17611. https://doi.org/10.1021/acs.jpcc.8b01949.

(41) Goetz, K. P.; Fonari, A.; Vermeulen, D.; Hu, P.; Jiang, H.; Diemer, P. J.; Ward, J. W.; Payne, M. E.; Day, C. S.; Kloc, C.; Coropceanu, V.; McNeil, L. E.; Jurchescu, O. D. Freezing-in Orientational Disorder Induces Crossover from Thermally-Activated to Temperature-Independent Transport in Organic Semiconductors. *Nat Commun* **2014**, *5* (1), 5642. https://doi.org/10.1038/ncomms6642.

(42) Musiienko, A.; Pipek, J.; Praus, P.; Brynza, M.; Belas, E.; Dryzhakov, B.; Du, M.-H.; Ahmadi, M.; Grill, R. Deciphering the Effect of Traps on Electronic Charge Transport Properties of Methylammonium Lead Tribromide Perovskite. *Sci Adv* **2020**, *6* (37). https://doi.org/10.1126/sciadv.abb6393.

(43) Wu, W.-Q.; Yang, Z.; Rudd, P. N.; Shao, Y.; Dai, X.; Wei, H.; Zhao, J.; Fang, Y.; Wang, Q.; Liu, Y.; Deng, Y.; Xiao, X.; Feng, Y.; Huang, J. Bilateral Alkylamine for Suppressing Charge Recombination and Improving Stability in Blade-Coated Perovskite Solar Cells. *Sci Adv* **2019**, *5* (3). https://doi.org/10.1126/sciadv.aav8925.

(44) Tan, H.; Jain, A.; Voznyy, O.; Lan, X.; García de Arquer, F. P.; Fan, J. Z.; Quintero-Bermudez, R.; Yuan, M.; Zhang, B.; Zhao, Y.; Fan, F.; Li, P.; Quan, L. N.; Zhao, Y.; Lu, Z.-H.; Yang, Z.; Hoogland, S.; Sargent, E. H. Efficient and Stable Solution-Processed

Planar Perovskite Solar Cells via Contact Passivation. *Science (1979)* **2017**, *355* (6326), 722–726. https://doi.org/10.1126/science.aai9081.

(45)   Zhao, D. W.; Sun, X. W.; Jiang, C. Y.; Kyaw, A. K. K.; Lo, G. Q.; Kwong, D. L. Efficient Tandem Organic Solar Cells with an Al/MoO3 Intermediate Layer. *Appl Phys Lett* **2008**, *93* (8), 083305. https://doi.org/10.1063/1.2976126.